Comparison of viscoelastic flows in two- and three-dimensional serpentine channels

Himani Garg[*] and Christer Fureby[†]
Department of Energy Sciences, Lund University, P. O. Box 118, SE-22100 Lund, Sweden

(Received 20 November 2023; accepted 8 May 2024; published 29 May 2024)

Polymer solutions in the dilute regime play a significant role in industrial applications. Due to the intricate rheological properties of these highly viscoelastic fluids, especially in complex flow geometries, a thorough numerical analysis of their flow dynamics is imperative. In this research, we present a numerical investigation of purely elastic instability occurring in two- and three-dimensional serpentine channels under conditions where fluid inertia is negligible and across a broad spectrum of polymer relaxation times. Our findings reveal a strong qualitative agreement between the existing experimental results obtained from dilute solutions of flexible polymers in microfluidic devices and the numerical simulations conducted in two and three dimensions using the Oldroyd-B model. Spatial flow observations and statistical analysis of temporal flow features indicate that this purely elastic turbulent flow exhibits nonhomogeneous, non-Gaussian, and anisotropic characteristics across all scales. Additionally, our comparison of two- and three-dimensional simulations demonstrates that the elastic instability is primarily driven by the curvature of the streamlines induced by the flow geometry, rather than the weak secondary flow in the azimuthal direction. Therefore, our two-dimensional numerical simulations successfully replicate, at least qualitatively, the features observed in three-dimensional experiments. Furthermore, spectral analysis suggests that, in comparison to elastic turbulence in the dilute regime, the range of scales for the excited fluctuations is narrower.

DOI: 10.1103/PhysRevE.109.055108

I. INTRODUCTION

Viscoelastic flows are commonly encountered in various scientific and industrial scenarios. These include secondary flows in blood and DNA suspensions, as well as in the manufacturing of polymeric products [1], particle focusing (i.e., the tendency of identical particles to align themselves to certain locations in a flow) [2], or cooling of electronics [3]. The flow of such fluids is complex and gives rise to instabilities that are unique to viscoelastic fluids. Under certain conditions, viscoelastic fluids exhibit non-Newtonian behavior, especially in dilute polymer solutions. Elastic forces become significant when polymer chains stretch due to fluid velocity gradients. When elasticity surpasses a critical value, these forces can trigger instabilities, causing irregular turbulence-like flow even at low Reynolds (Re) numbers, a phenomenon known as elastic turbulence [4–10]. Elastic turbulence is marked by rapid growth in the largest Lyapunov exponent [7,11,12] and exhibits power-law behavior in spatial and temporal kinetic energy spectra, indicating a range of active scales in the flow [4,8,13]. Despite its resemblance to turbulent flow, elastic turbulence offers promising opportunities for improving mixing [5], enhancing heat transfer [14,15], and aiding in oil recovery [16].

The phenomenon of elastic turbulence has been extensively researched. A concise summary of the main theoretical findings on elastic turbulence is provided by Fouxon and Lebedev [17], further explored by Brughelea *et al.* [8], Soulies *et al.* [9], and Steinberg [13]. However, the lack of experimental techniques for *in situ* measurement of elastic stresses poses a significant challenge to the much-needed understanding of the turbulent-like dynamics in elastic turbulence. As a solution, recent two-dimensional (2D) numerical simulations have demonstrated the possibility of accurately reproducing the essential characteristics of elastic turbulence through a simplified flow model of a highly elastic polymer solution at low Re numbers. These investigations focused on the Oldroyd-B model dynamics in a 2D, inhomogeneous, periodic, Kolmogorov flow setup [11,18–20]. A recent numerical study by Garg *et al.* [20] focused on the statistical properties of elastic turbulence in the same system, examining single- and multipoint statistics in both temporal and spatial domains. Their findings indicate nearly identical scaling in both temporal and spatial spectra of velocity fluctuations, with an exponent of approximately -4. In contrast, van Buel *et al.* [21] found significant scaling exponent variations in the radial direction in Taylor-Couette flow.

Since both theory and experiments deal with a fully 3D flow, 2D simulations cannot represent vortex stretching and other inherently 3D flow physics phenomena. Therefore, 2D simulations should albeit their extensive use in elastic turbulence be availded. Recent studies have started exploring 3D elastic turbulence flows, particularly in Taylor-Couette flows [22]. While studies using 2D simulations and simplified

[*]himani.garg@energy.lth.se
[†]christer.fureby@energy.lth.se

models have shown outcomes strikingly similar to experimental findings, the reasons for this are unclear. Also, there has not been a detailed comparison of elastic turbulence flows in both 2D and 3D. This highlights the need for future research to directly compare the two and fill this gap.

To the best of our knowledge, no existing literature directly compares 2D and 3D numerical simulations of elastic turbulence. In this study, we analyze the statistical characteristics of elastic turbulence in 2D and 3D microserpentine channels by directly comparing them, inspired by experiments [23]. Our investigation primarily focuses on spatial flow features and single-point statistics in the temporal domain. We aim to distinguish between flow in 2D and 3D, explaining their similarities and differences. Additionally, we quantify the homogeneity and isotropy of velocity fluctuations, emphasizing the role of dimensionality. Our analysis covers various flow properties, including strain rate, vorticity, and topology factor, as well as velocity fluctuation power spectra and second-order structure functions of velocity increments at different Weissenberg numbers, Wi, comparing elastic and viscous forces. Furthermore, we explore the interplay between polymer dynamics and flow geometry, analyzing the Lumley triangle.

The paper is organized into five main sections, with the remaining sections following as outlined: Sections II and III describe the methodology used for the numerical simulations and provide details regarding boundary conditions and dimensionless numbers used in the analysis. Section IV presents the results and discussions, and, finally, the conclusions are drawn in Sec. V.

II. VISCOELASTIC CONSTITUTIVE EQUATION AND NUMERICAL METHODOLOGY

Based on the continuum hypothesis and incompressible flow condition, the velocity $\boldsymbol{v}\ (\boldsymbol{x}, t)$ at position $\boldsymbol{x}$ and time t evolves according to the mass and momentum equations given by

$$\nabla \cdot \boldsymbol{v} = 0, \tag{1}$$

$$\rho\left[\frac{\partial \boldsymbol{v}}{\partial t} + \nabla \cdot (\boldsymbol{v} \otimes \boldsymbol{v})\right] = -\nabla p + \nabla \cdot \boldsymbol{\tau}, \tag{2}$$

where ρ is the fluid density, p the fluid pressure, and $\boldsymbol{\tau} = \boldsymbol{\tau}_s + \boldsymbol{\tau}_p$ the fluid stress tensor which consists of both solvent ($\boldsymbol{\tau}_s$) and elastic ($\boldsymbol{\tau}_p$) solute contributions.

In the framework of the Oldroyd-B model [24], $\boldsymbol{\tau}_s = 2\eta_s \boldsymbol{D}$, where η_s is the zero-shear dynamic viscosity of the solvent, $\boldsymbol{D} = \frac{1}{2}[\nabla \boldsymbol{v} + (\nabla \boldsymbol{v})^T]$ the strain-rate tensor, and $\boldsymbol{\tau}_p$ the elastic solute stress tensor and is expressed by the following constitutive equation following Oldroyd [25]:

$$\boldsymbol{\tau}_p + \lambda\left\{\frac{\partial \boldsymbol{\tau}_p}{\partial t} + \nabla \cdot (\boldsymbol{v} \otimes \boldsymbol{\tau}_p) - [(\nabla \boldsymbol{v})^T \otimes \boldsymbol{\tau}_p] - (\boldsymbol{\tau}_p \otimes \nabla \boldsymbol{v})\right\} = 2\eta_p \boldsymbol{D}, \tag{3}$$

where λ is the largest polymer relaxation time and η_p is the polymer contribution to viscosity. Equation (3) can also be written in terms of conformation tensor, $\boldsymbol{\sigma} = \frac{\lambda}{\eta_p}\tau_p + \mathbf{I}$, as follows:

$$\frac{\partial \boldsymbol{\sigma}}{\partial t} + \nabla \cdot (\boldsymbol{v} \otimes \boldsymbol{\sigma}) - [(\nabla \boldsymbol{v})^T \otimes \boldsymbol{\sigma}] - (\boldsymbol{\sigma} \otimes \nabla \boldsymbol{v}) = \frac{1}{\lambda}(\mathbf{I} - \boldsymbol{\sigma}), \tag{4}$$

where $\mathbf{I}$ is the identity tensor.

Although the Oldroyd-B model exhibits an unbounded steady-state extensional viscosity above a critical strain-rate ($1/2\lambda$), in shear-dominated serpentine channel geometries, such deficiencies are unimportant, and it is arguable the simplest constitutive equation that can capture many aspects if highly elastic flows [19,20,26]. The Oldroyd-B model emerges as a simplified version within certain limits of the more comprehensive viscoelastic models, such as the FENE-P, Giesekus, and Phan-Thien-Tanner models (see, e.g., Bird *et al.* [24]). This simplified representation makes it particularly suitable for fundamental studies of viscoelastic fluid behavior.

Equations (1) through (3) are numerically integrated using the open-source solver RheoTool [27], which was developed within the OpenFOAM framework [28]. This solver relies on a finite-volume discretization method and implements the log-conformation technique [29] to mitigate numerical instabilities associated with high values of Wi. It is worth noting that we do not introduce polymer-stress diffusion in this context. For solving the components of the polymeric stress tensor, we employ a biconjugate gradient solver in conjunction with a diagonal incomplete LU preconditioner (DILU-PBiCG). The velocity and pressure fields are solved using a conjugate gradient solver coupled with a diagonal incomplete Cholesky preconditioner (DIC-PCG). We employ a second-order backward scheme for time discretization. The convective fluxes are discretized using the third-order accurate CUBISTA scheme for the momentum and energy conservation equations [30]. Additionally, a second-order-accurate scheme is employed for discretizing the convective term in the conformation tensor transport equation.

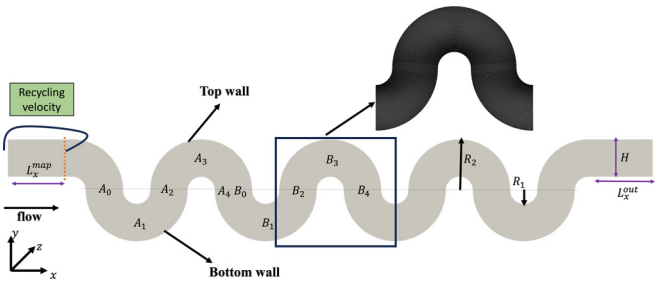

FIG. 1. Schematic of the microfluidic domain with constant inner and outer curvatures. $\boldsymbol{x}$ is the primary flow direction, H is the channel height, and R_1 and R_2 are the inner and outer radius where the origin is taken as the inner edge of each loop. A_i's and B_i's correspond to probes location nomenclature.

III. FLOW GEOMETRY, DIMENSIONLESS NUMBERS, BOUNDARY CONDITION, AND COMPUTATIONAL GRIDS

In this study, we examine the flow of elastic turbulence within a serpentine microchannel, using both 2D and 3D geometry setups. The microchannel configuration is inspired by Ducloué *et al.* [31] and is shown from the side in Fig. 1.

The fluid is assumed to be incompressible and inertialess. For both the 2D and 3D simulations, the microchannel consists of three sections: an initial planar channel with a length of $L_x^{\text{in}} = 190$ μm, followed by a series of $N = 7$ connected half-circular rings, and last followed by another planar channel with a length of $L_x^{\text{out}} = 190$ μm (see Fig. 1). The inner and outer radii of these rings are $R_1 = 40$ μm and $R_2 = 150$ μm, respectively. The height of the channel is $H = R_2 - R_1 = 110$ μm, and the width is $W = 65$ μm (applicable to the 3D case). The geometric aspect ratio, which is pertinent to the onset of the primary elastic instability [23,31], is defined as $a = R_1/H = 0.364$. For the presentation of qualitative results, we focus on the section between the bends in the second and sixth half loops. On the other hand, for quantitative findings, we concentrate on the bend in the fourth half loop to eliminate any biases arising from the proximity to the inlet and outlet.

It is important to clarify that the coordinate system (x, y, z) is fixed in space. However, for the sake of consistency, we will consistently refer to the velocity components in the following manner: the direction aligned with the flow is denoted as u, the wall-normal or transverse direction is represented as v, and the spanwise direction is indicated as w. Consequently, the streamwise velocity component, u, for example, is aligned exclusively with the x direction in the straight inlet and outlet channels, as well as at locations $A_2, A_4/B_0$, and so forth. As a result, at location A_0, the wall-normal (or transverse) velocity corresponds to the velocity component in the y direction. However, at A_1, following a 90° change in the flow direction, it corresponds to the component in the x direction. In contrast, the velocity in the spanwise direction (often referred to as the "neutral" or "spanwise" direction) is consistently designated as w.

A crucial parameter in our analysis is the viscosity ratio, $\beta = \eta_s/(\eta_s + \eta_p)$, which is inversely proportional to the polymer concentration. For a given value of β, the primary controlling parameters in the dynamics, as described by Eqs. (2) and (3), are Re and Wi. The Reynolds number is defined as $\text{Re} = \rho U_{\max} H/(\eta_s + \eta_p)$, where $U_{\max}$ represents the maximum velocity at the inlet. The Weissenberg number is given by $\text{Wi} = \lambda U_{\max}/H$, with λ representing the polymer relaxation time. We also introduce a critical Weissenberg number, denoted as Wi_{crit}, which serves as the threshold value of Wi at which elastic instabilities begin to manifest in a viscoelastic fluid. It is worth noting that, in our current investigation, $\text{Wi}_{\text{crit}}^{\text{2D}}$ is approximately in the range of 3–4 [32], while $\text{Wi}_{\text{crit}}^{\text{3D}}$ is approximately 2–3. These values represent the critical Wi numbers for 2D and 3D setups, respectively, and will be discussed in later sections. Additionally, we have removed the convective term from Eq. (2) to ensure that inertial forces are truly negligible in our analysis.

In our current investigation, we maintain the values of $\beta = 0.8$ [23] and Re number at a constant level. This is done to solely explore the impact of varying Wi within the range of 0–20 on flow properties. The value of Re number is set to approximately $\sim 10^{-3}$ to ensure we operate within the low Re number regime, where the flow of a Newtonian fluid is inherently laminar. It is important to note that at $\text{Wi} = 0$, we are dealing with a Newtonian laminar flow. For our simulations, the time step is determined as $\Delta t = 0.1 \times \min(\lambda, t_c, t_d)$, where $t_c = H/U$ represents the convective time step, and $t_d = H^2/\nu$ corresponds to the diffusive time step. In a prior study [32], we conducted a comprehensive analysis to assess the mesh independence of the curvilinear 2D microserpentine channel at $\text{Wi} = 5$. Based on the mesh sensitivity findings by Garg *et al.* [32], we created two computational domains. The first one is designed for the 2D serpentine channel with a grid size of $N_x \times N_y = 4480 \times 42$ cells, while the second one accommodates the 3D serpentine channel with $N_x \times N_y \times N_z = 4480 \times 42 \times 25$ cells.

At the inlet of the channel, we impose a parabolic velocity profile, which can be expressed as $u(y) = U_{\max}(1 - y^2)$. We apply a zero-Neumann boundary condition for the pressure field at the inlet, while the polymeric extra stresses, denoted as $\boldsymbol{\tau}_p$, are set to zero. Moving to the outlet, we implement a zero-Dirichlet boundary condition for the pressure, along with a zero-Neumann condition for both velocity and polymer extra stresses. For the channel walls, we enforce a no-slip condition for the velocity field, ensuring that the fluid velocity at the wall is zero. Additionally, we utilize a linear extrapolation technique for the polymer extra stresses at the walls. As for the initial conditions, both the velocity and stress fields are initialized with no flow.

In experimental setups, the channel is typically quite long, often consisting of roughly 200 turns, to allow the flow to fully develop, especially in the regime of high Wi numbers. However, when conducting simulations, the use of small time steps can make it impractical to model such extensive geometries. To ensure that the selected channel length is sufficient for the flow to reach a fully developed state, we have estimated the development lengths for laminar base flow using the correlation $L_{\text{dev}}^{\text{lam}}/H = 0.06\text{Re}$ [33]. In our current simulations, $L_{\text{dev}}^{\text{lam}}$ is approximately 44 nm [32]. This suggests that $L_{\text{dev}}^{\text{lam}}$ is significantly smaller than the total channel length, denoted as $L_x = 1.9$ mm. On the other hand, when we reached the fully developed elastic turbulence regime, in the absence of a theoretical prediction, we measured the average velocity fluctuations at different points along the channel (as illustrated in Fig. 1). The results revealed that for both 2D and 3D simulations, the velocity fluctuations stabilized after the third semiturn, suggesting that the channel length we used was adequate. Therefore, it is safe to conclude that the chosen channel length is more than adequate for the flow to reach a fully developed state. Furthermore, to ensure that the numerical results are independent of entrance effects, we establish fully developed flow within the elastic turbulence regime by recycling the velocity field at the inlet from an arbitrary plane situated at a distance of $L_x^{\text{map}} = 150$ μm downstream of the inlet. Cyclic boundary conditions are applied for the inlet and the arbitrary plane downstream, enabling the recycled velocity to flow continuously into the remaining portion of the channel and progress toward the outlet. It is essential to note that recycling is primarily implemented for cases involving large values of Wi.

IV. RESULTS AND DISCUSSIONS

A. Fluctuating velocity

To investigate the statistical features of elastic turbulence, it is convenient to analyze the fluctuating component of the

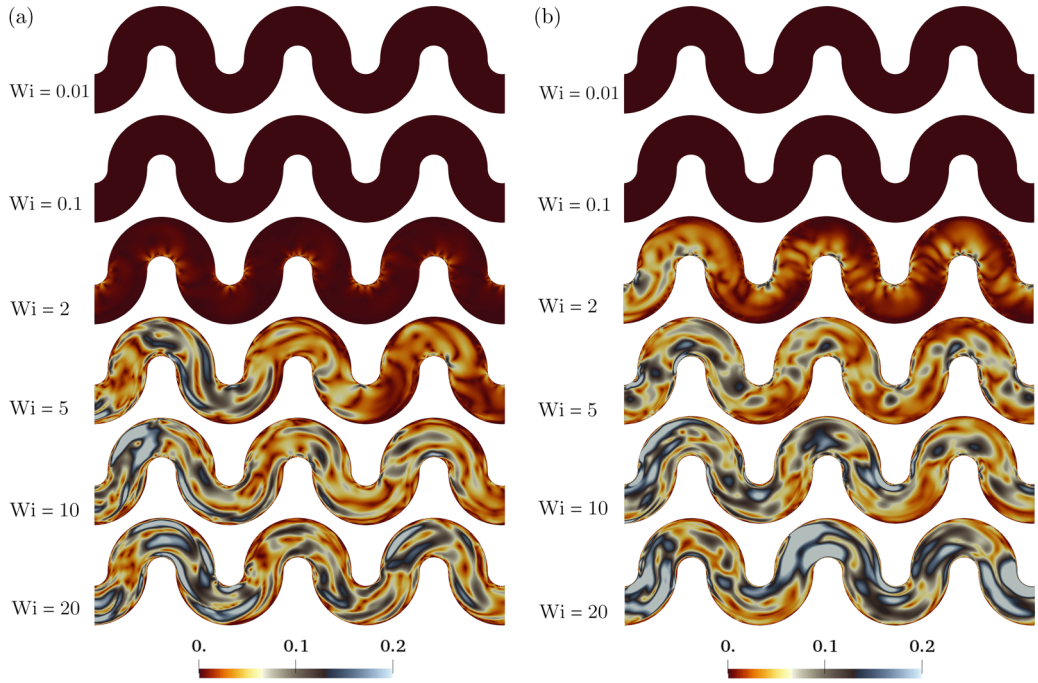

FIG. 2. The pseudocolor plots, in (a) 2D and (b) 3D serpentine channel, correspond to instantaneous snapshots of velocity fluctuation magnitude, $|\boldsymbol{v}|$, as a function of Wi = 0.01–20.

velocity, defined as $\boldsymbol{v}'(x, y, z, t) = \boldsymbol{v}(x, y, z, t) - \langle \boldsymbol{v}(x, y, z, t) \rangle$, where $\langle \dots \rangle$ represents the time average. In the 2D case, the flow is considered invariant with respect to the z coordinate.

In Fig. 2, we compare the instantaneous velocity fluctuation magnitudes between 2D and 3D simulations as a function of Wi. Our analysis in Fig. 2 reveals that the velocity fluctuation magnitudes remain negligible for Wi $<<$ 2 and increase as Wi increases. Additionally, the velocity fluctuation magnitudes are slightly higher in the 3D case compared to the 2D case. This observation suggests an elevated level of turbulence and improved mixing and dispersion in 3D elastic turbulence. The presence of an additional dimension allows for more complex flow structures and interactions, resulting in stronger velocity fluctuations. This underscores the influence of the third dimension and the potential role of secondary flow and viscoelastic effects in shaping the characteristics of elastic turbulent flow. Moreover, in qualitative terms, these results indicate that $\mathrm{Wi}_{\mathrm{crit}}^{\mathrm{2D}}$ is approximately in the range of 3–4, while $\mathrm{Wi}_{\mathrm{crit}}^{\mathrm{3D}}$ falls within the range of 2–3 for 2D and 3D simulations, respectively.

To gain a more quantitative understanding of the effect of Wi on the initiation of velocity fluctuations, we provide an example of data obtained from pointlike probes in Fig. 3 for both the 2D and 3D cases. This figure displays the time series of the fluctuations in the streamwise velocity component, u', the cross-stream component, v', and the spanwise component, w' (in the case of 3D), all normalized by the mean flow intensity. These data are collected at one selected probe location, specifically, B_3 as indicated in Fig. 1, for different values of Wi, such as Wi = 0.01, 5, 10, and 20. In these plots, time is normalized by the polymer relaxation time, denoted as λ. It is important to note that the data presented here correspond to a subset of the complete time series, which extends up to 100λ. Clearly, for Wi = 0.01, the fluctuations are negligible, and with increasing Wi, we observe the onset of elastic instabilities. However, for Wi $\geqslant$ 5, it becomes challenging to distinguish the impact of Wi on velocity fluctuations, as all the curves exhibit a similar behavior. It is worth noting the varying intensities of fluctuations in the x, y, and z directions.

Additionally, we calculated the autocorrelation times, τ_i^c, from the autocorrelation functions of each velocity fluctuation component [20]. In our 2D simulations, we found that the values of $\tau_{u'}^c/\tau$ and $\tau_{v'}^c/\tau$ during fully developed elastic turbulence regime ranged between 9.625–3.146 and 10.903–2.970, respectively. For the 3D case, these values were between 9.008–2.728 and 9.368–2.521, respectively. These findings differ from the experimental results of Soulies *et al.* [9], where $\tau_{u'}^c/\tau = 190$ and $\tau_{v'}^c/\tau = 13$. However, our results are in line with the findings of experiments conducted on millimeter serpentine channel [34] in terms of order of magnitude at high Wi. The significant variability observed among different experimental results, theoretical predictions, and numerical simulations need further investigation, but this is beyond the scope of our current study.

In Fig. 4(a), we present the time-averaged magnitude of velocity fluctuations, normalized by the mean flow, as a function of the Wi number for both 2D and 3D cases. We observe three distinct flow regimes: For Wi $<$ 3, turbulence intensity is negligibly small, indicating a laminar flow regime. In the range of 3 $<$ Wi $\leqslant$ 5, there is a sharp increase, signifying the onset of elastic turbulence. At this point, we refer to Wi as the critical Weissenberg number ($\mathrm{Wi}_{\mathrm{crit}}$). Finally, for 5 $<$ Wi $\leqslant$ 20, there is a continuous increase approaching asymptotic values of $|\boldsymbol{v}'|/U = 0.125$ for the 2D case and $|\boldsymbol{v}'|/U = 0.18$ for the 3D case, indicating a fully developed elastic turbulence regime. In qualitative terms, the 2D and 3D simulation results exhibit similar behavior but differ in absolute values. To compare the

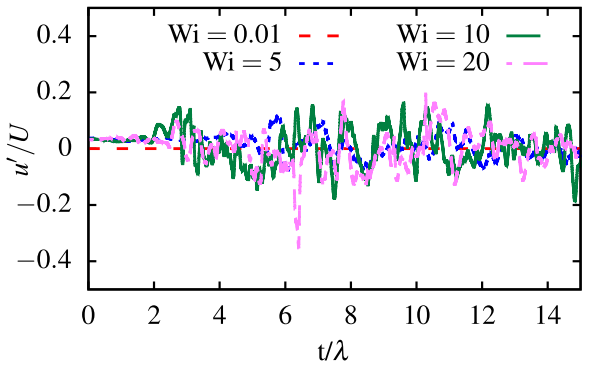

(a) u'/U (2D simulations)

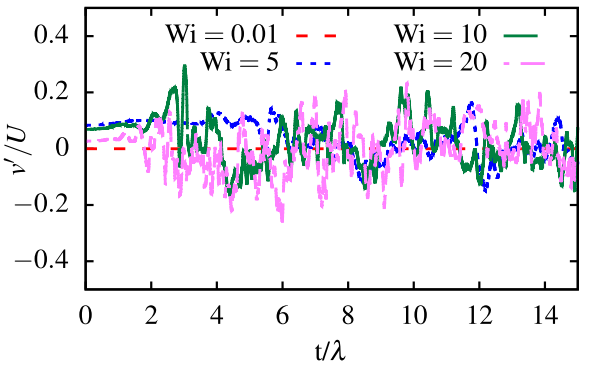

(b) v'/U (2D simulations)

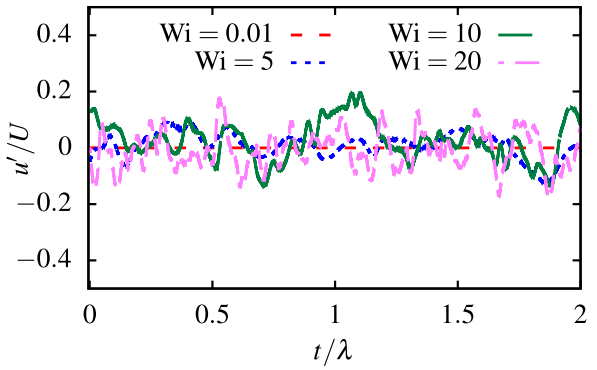

(c) u'/U (3D simulations)

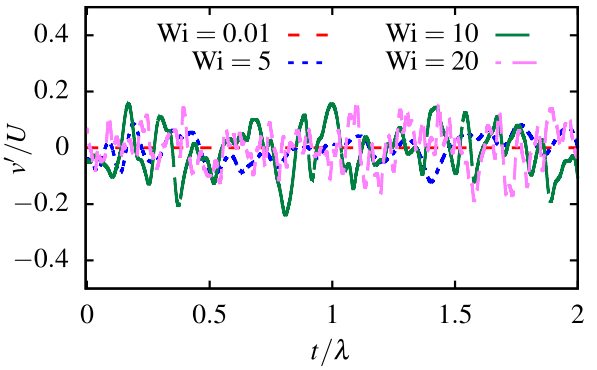

(d) v'/U (3D simulations)

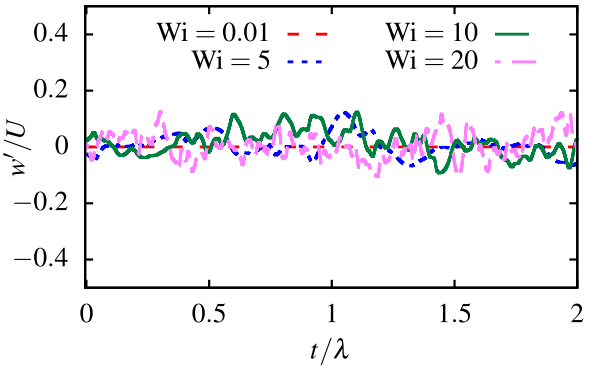

(e) w'/U (3D simulations)

FIG. 3. Time series of velocity fluctuations [(a) and (b)] for 2D and [(c)–(e)] for 3D simulation cases. All results are normalized by the mean flow amplitude, U, at Wi = 0.01, 5, 10, and 20. To ease visualization, only a short subset of the full data set (which reaches $t/\lambda = 100$) is shown.

similarities between 2D and 3D simulations, we performed data fitting using a $a * \mathrm{Wi}^b$ function and obtained scaling exponents for each case. In the laminar regime, for both 2D and 3D cases, we found that $|v'/U|$ scales approximately as $\mathrm{Wi}^{1.29}$ and $\mathrm{Wi}^{2.15}$ respectively. In the fully developed elastic turbulence regime, $|v'/U|$ scales approximately as $\mathrm{Wi}^{0.5}$ and $\mathrm{Wi}^{0.52}$ respectively. The critical value of Wi^{3D}_{crit}, approximately 3, is consistent with experimental observations in serpentine channel flow as reported in Refs. [6] and [7]. However, Wi^{2D}_{crit}, estimated at approximately 4–5, appears to be slightly overestimated compared to experiments and 3D simulations. Similarly, in Fig. 4(b), the average value of the trace of the polymer conformation tensor, $\mathrm{tr}(\boldsymbol{\sigma})$, is plotted. In both cases, $\mathrm{tr}(\boldsymbol{\sigma})$ increases with increasing Wi number. For the 2D case, the absolute stretching of the polymers is roughly two times smaller compared to the 3D case, especially in the range of large Wi numbers. This could be associated with the occurrence of vortex stretching, a phenomenon that is not present in the 2D case, which will be discussed later in detail. Moreover, we observed that for $\mathrm{tr}(\boldsymbol{\sigma})$, the scaling is $\mathrm{Wi}^{1.06}$ for 2D simulations and $\mathrm{Wi}^{1.12}$ for 3D simulations. The difference in scaling between the two is small.

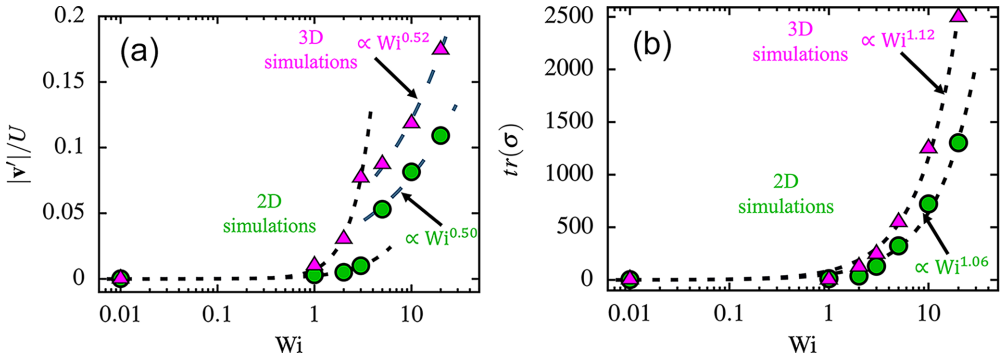

FIG. 4. Comparison of (a) velocity fluctuations magnitude normalized by U and (b) the trace of the polymer conformation tensor, as a function of Wi number, for 2D and 3D simulations.

B. Mean flow profiles

Figure 5 presents the time-averaged streamwise velocity profile along the centerline (shown in Fig. 1). In this figure, y represents the wall-normal direction, and x denotes the main velocity direction. The figure is plotted in a way that the $y = 0$ position corresponds to the inner edge at $x/W = 6.9$. For comparison sake, the profiles from the Newtonian laminar case are also extracted for both 2D and 3D cases. In Figs. 5(a) and 5(b), the streamwise velocity components for 2D and 3D flow setup are shown, respectively. First, it is noticeable that the Newtonian simulations and the small Weissenberg regime ($\mathrm{Wi} < \mathrm{Wi_{crit}}$) agree well, but a slight asymmetry towards the inner wall is present. Similar observations have been made and discussed in previous studies [23]. Second, the effect of elasticity on the main velocity component is relatively stable, but on examination of the profiles around the maximum of $\langle u_x \rangle$ (not shown in this figure), it is apparent that elasticity enhances this asymmetry by shifting the velocity peak away from the center of the channel. The shift in velocity peak becomes prominent in 3D cases compared to 2D.

C. Polymer stretching

Figures 6 and 7 exhibit a momentary snapshot of the polymer conformation tensor's trace, $\mathrm{tr}(\boldsymbol{\sigma})$, the strain-rate tensor's magnitude, $\|\boldsymbol{D}\|$, and in-plane vorticity, $\omega_z = \partial v/\partial x - \partial u/\partial y$, for 2D and 3D (only z component) cases at $\mathrm{Wi} = 0.01, 0.1, 2, 5, 10,$ and 20, respectively. The trace of $\boldsymbol{\sigma}$ provides information about the average alignment and stretching of polymer chains in all directions. These visualizations enable us to understand the degree of polymer stretching easily, the preferred elongation regions for polymers, and the emergence of secondary vortical structures on top of the unidirectional mean background flow as Wi increases. When $\mathrm{Wi} < \mathrm{Wi_{crit}}$, the flow is laminar, and the polymers assume their coiled configuration, as evidenced by the clear dis-

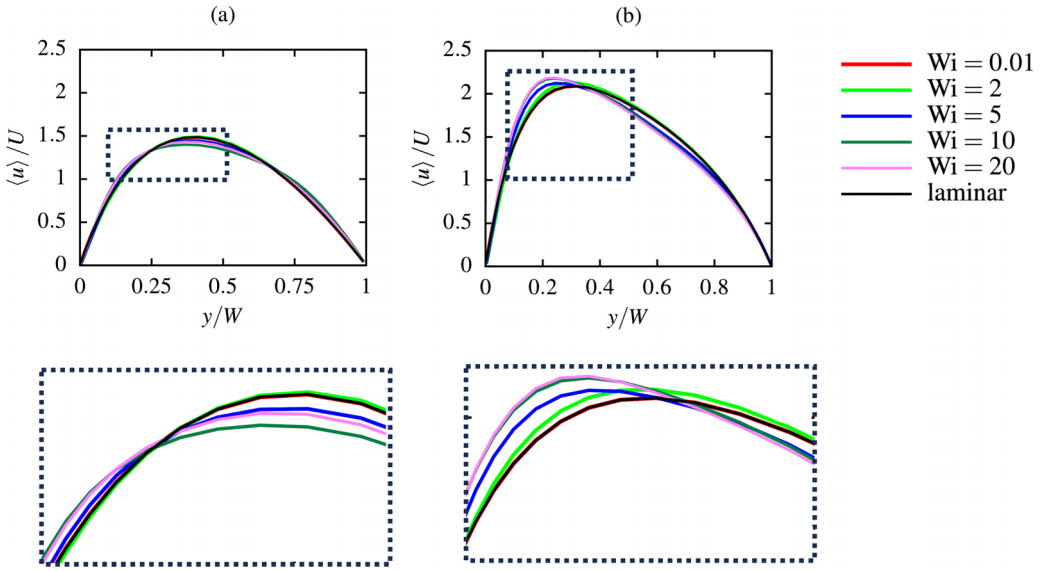

FIG. 5. Mean flow profile, $\langle u \rangle$, extracted along the mid-height of the channel at the central half-bend as a function of Weissenberg number, $\mathrm{Wi} = 0$–20, for (a) 2D and (b) 3D simulations of the microserpentine channel. All profiles are normalized by the mean flow amplitude, U. Some zooms are also included for enhanced visualizations.

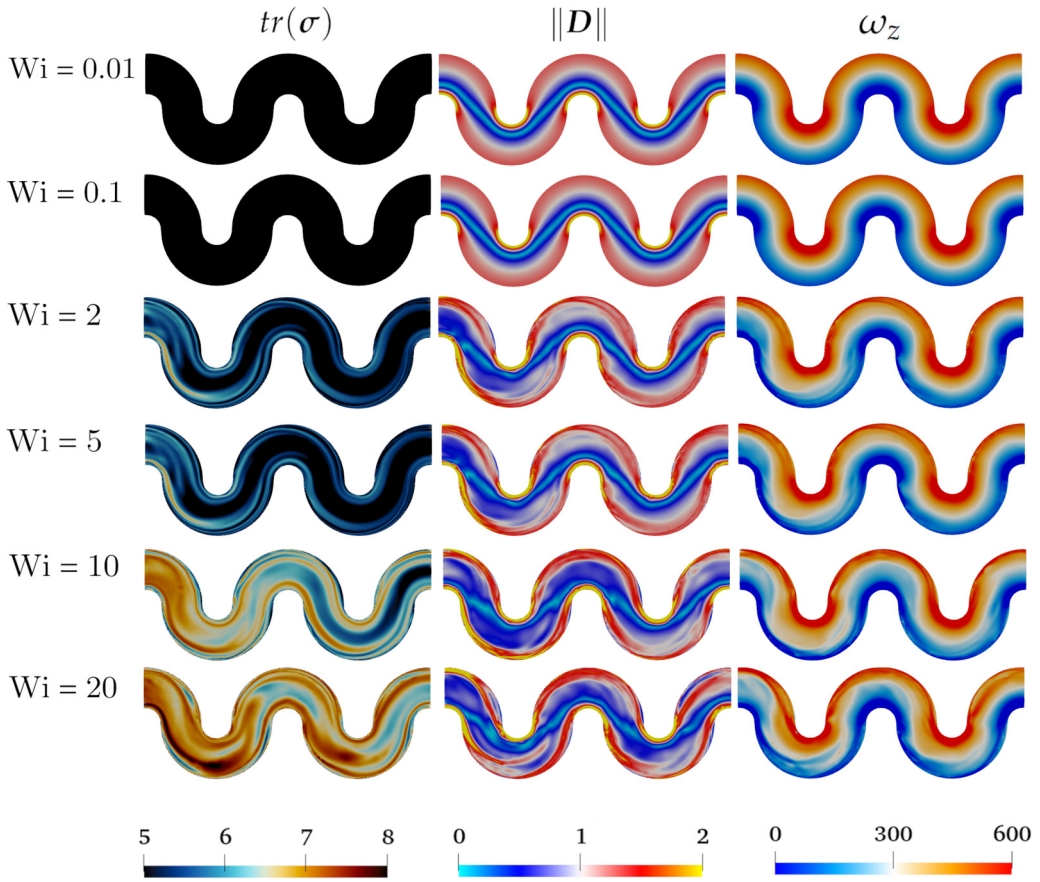

FIG. 6. The pseudocolor plots, in 2D serpentine channel, correspond to instantaneous snapshots of the trace of polymer conformation tensor, tr($\boldsymbol{\sigma}$), magnitude of the strain-rate tensor, $\|\boldsymbol{D}\|$, and vorticity, $\omega_z = \partial v/\partial x - \partial u/\partial y$, as a function of Weissenberg number, Wi = 0.01–20.

tinctions between stretching, elongation, and extension flow regions.

Interestingly, these results reveal that polymers are maximally stretched in the preferential regions of high strain-rate tensor, which is consistent with previous numerical results [19]. In qualitative terms, we once again observe that the onset of purely elastic instabilities happens earlier in the 3D setup compared to the 2D simulations. However, from these instantaneous plots, it is not immediately evident whether the third dimension significantly influences the features of elastic turbulent flow. To address this question, we conducted a comprehensive analysis of several other parameters to initially characterize the flow in both 2D and 3D simulations, which will be presented in the subsequent section.

D. Flow topology and its impact on polymer behavior and flow features

Due to the curvature of the channels, the flow becomes weakly asymmetric, and the location of the maximum velocity occurs slightly closer to the inner wall. In between the two half-circles, the flow regains symmetry before becoming asymmetric towards the other side in the next half-circles. This effect is visible in the snapshots in Fig. 8. The flow of a semidilute polymer solution is complex due to the interplay between fluid and flow properties. To understand the unstable flow behavior, which depends on the molecular behavior of the polymers in 2D and 3D flow geometries, we must first gain insight into its origin. Previous studies have shown that the purely elastic instability in polymer solutions is governed by polymer deformation dynamics, which are highly influenced by the flow type [35,36]. Thus, the flow type in the geometry can be considered a crucial factor in determining polymer behavior [37]. We consider a practical dimensionless number to define the flow type, a.k.a. topology factor defined as

$$\zeta = \frac{\|\boldsymbol{D}\| - \|\boldsymbol{\Omega}\|}{\|\boldsymbol{D}\| + \|\boldsymbol{\Omega}\|}, \tag{5}$$

where $\|\boldsymbol{\Omega}\|$ is the magnitude of rate of rotation tensor $\Omega_{ij} = (\partial v_i/\partial x_j - \partial v_j/\partial x_i)$ [38]. The polymers undergo intrinsic deformation under different flow types. At low to moderate shear rates, the polymers remain coiled and align with the flow direction at high shear rates. Under extensional flow, the polymers stretch, while rotational flow tends to restore them to their coiled state [37].

In this study, the topology factor distribution is calculated for both 2D and 3D cases at two different values of the Weissenberg number, Wi = 0.01 < Wi_{crit} and Wi = 20 > Wi_{crit}, and is shown in Fig. 8. Below the onset of purely elastic instability, Wi < Wi_{crit}, the flow appears to be mainly shear dominant, with orderly alternating regions of shear, extensional, and rotational flows. For Wi > Wi_{crit}, the results in 2D and 3D differ. For 2D simulations in a fully developed

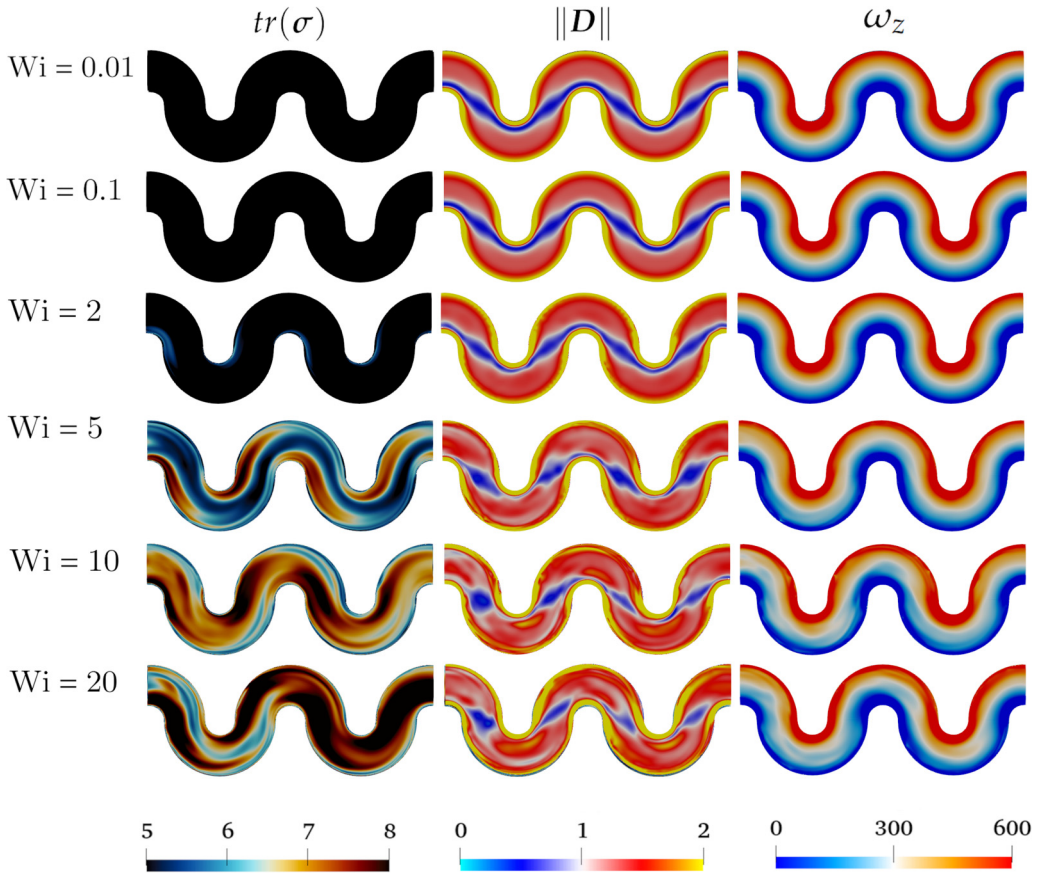

FIG. 7. The pseudocolor plots, in 3D serpentine channel, correspond to instantaneous snapshots of the trace of polymer conformation tensor, tr($\boldsymbol{\sigma}$), magnitude of the strain-rate tensor, $\|\boldsymbol{D}\|$, and z component of vorticity field, $\omega_z = \partial v/\partial x - \partial u/\partial y$, as a function of Weissenberg number, Wi = 0.01–20.

elastic turbulence regime, the orderly distribution of flow types suggests that the purely elastic turbulence flow is isotropic. In contrast, in 3D, these regions are less distinct, and the flow types are randomly distributed, resulting in spatial inhomogeneity of the flow. The significant contribution of randomly distributed rotational flow suggested anisotropic flow in 3D. Further details on the isotropic nature of the flow will be discussed later. These results, particularly in the 3D case, align with experimental observations [39].

E. Vortex stretching and polymeric feedback

So far, flow characterization shows some similarities and differences between 2D and 3D depending on the flow feature we are looking at. The striking similarity between 2D and 3D is surprising, as we know in 3D simulations, vortex stretching is prominent, which is absent in 2D simulations. To uncover the actual reason behind this, we looked at the vorticity transport equation:

$$\frac{\partial \boldsymbol{\omega}}{\partial t} + \boldsymbol{v}\cdot\nabla\boldsymbol{\omega} = \boldsymbol{\omega}\cdot\nabla\boldsymbol{v} + \nabla\cdot\left(\frac{\eta_s}{\rho}\nabla\boldsymbol{\omega}\right) + \frac{1}{\rho}[\nabla\times(\nabla\cdot\boldsymbol{\tau_p})]. \tag{6}$$

The first, second, and third terms on the right-hand side of Eq. (6) represents vortex stretching, VS, vorticity diffusion, VD, and polymeric feedback term, FT, respectively.

In our 3D simulations, we have graphed the values of these parameters along the central axis of the serpentine channel for various Wi values, as shown in Fig. 9. As expected, as the Wi value increases, both the magnitudes of VS and FT also increase. However, what is particularly noteworthy is that the order of magnitude of VS is notably smaller than that of FT. Note that the magnitude of VD is also examined and found to be several orders smaller than the FT [FT $\approx O(10^5) \times$ VS], hence not included in these plots. These observations imply that, in 3D simulations, the polymeric feedback term predominates despite the presence of vortex stretching. These results demonstrate that the elastic instability is primarily driven by the curvature of the streamlines induced by the flow geometry rather than the weak secondary flow in the azimuthal direction. This finding may provide an explanation for the significant similarities observed between the 2D elastic turbulence simulations and 3D experimental results.

Additionally, we have depicted spatially averaged values of FT for both 2D and 3D simulations, as well as VS for 3D simulations, in Fig. 10. A discernible increasing trend of FT (in both 2D and 3D simulations) and VS with an increasing Wi number is evident. Consistent with previous findings, the absolute value of FT in 2D simulations is notably smaller than in 3D simulations, particularly in the fully developed elastic turbulence regime. These discrepancies may be attributed to the absence of vortex stretching. It is conceivable that in

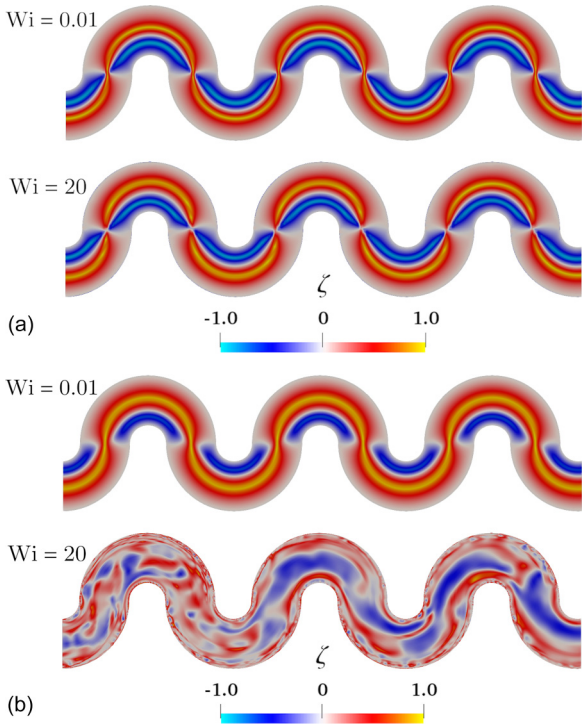

FIG. 8. Local distribution of the topology factor, ζ, along the (a) two-dimensional and (b) three-dimensional serpentine channel at Wi = 0.01 (top) and Wi = 20 (bottom). The value of $\zeta = -1.0$ indicates a pure rotational flow, $\zeta = 0.0$, a pure shear flow, and $\zeta = 1.0$, a pure extensional flow.

3D simulations, the interplay between the VS term and the FT term leads to a more significant extension of polymer molecules and, consequently, larger values of FT compared to 2D simulations. Moreover, we performed data fitting using a $a * \mathrm{Wi}^b$ function and obtained scaling exponents for each case. In both 2D and 3D cases, we found that FT scales approximately as $\mathrm{Wi}^{1.32}$ and $\mathrm{Wi}^{1.43}$ respectively and for 3D case VS scales around $\mathrm{Wi}^{1.74}$. It is worth noting that, to the best of the authors' knowledge, these results are being presented for the first time. To provide more concrete insights, we advocate for future in-depth investigations that specifically examine the relationship between vortex stretching and polymer feedback terms by comparing 2D and 3D simulations.

F. Spectra of velocity fluctuations

By utilizing fixed-point temporal measurements, we calculate power spectra of velocity fluctuations in the frequency domain, denoted as f. These data are averaged across all probe locations to ensure statistically robust results. In line with earlier investigations [5,6,20], we transform the frequency domain into the spatial domain, making an assumption based on the validity of Taylor's frozen hypothesis (though the need for verification remains for future studies). However, it is essential to exercise caution regarding the assumption of Taylor's hypothesis's validity, as discussed in the work of Garg *et al.* [20]. For 2D simulations, the resulting spectra, represented as $E_{i'}$, for both velocity fluctuation components within the elastic turbulence regime, are presented in Figs. 11(a) and 11(b). Regardless of the specific flow component and Wi value considered, we identify power-law decaying spectra with a common exponent of $\alpha = 4$, expressed as $E_{i'}(f) \sim f^{-\alpha}$.

Furthermore, in the context of 3D simulations, we present the resulting spectra, denoted as $E_{i'}$, where $i = u, v, w$, encompassing all velocity fluctuation components within the elastic turbulence regime. These spectra are displayed in Figs. 12(a)–12(c). Regardless of the specific Wi considered, we observe power-law decaying spectra for u' and w' components, characterized by $E_{i'}(f) \sim f^{-\alpha}$, with a common exponent α falling in the range of 3.1 to 3.8. The distinct scaling behaviors observed in the velocity fluctuation components in 3D simulations can also be understood in the context of the vorticity equation. In the limit of vanishing Re number, a complex interplay emerges between the vortex stretching term $\boldsymbol{\nabla} \cdot (\boldsymbol{\omega} \otimes \boldsymbol{v})$ and the nonlinear contribution of viscoelastic stresses $\boldsymbol{\nabla} \times (\boldsymbol{\nabla} \cdot \boldsymbol{\tau_p})/\rho$, as demonstrated previously. In both scenarios, the scaling range extends to slightly less than two decades for the temporal spectra, a trend consistent with previous numerical studies [11,20,40]. Furthermore, we observe that similar steep spectra have been documented in experiments [5–9], in the frequency domain and theoretically predicted, assuming homogeneity and isotropy, in the wavenumber domain [17]. Notably, the spectra for 2D simulations exhibit steeper characteristics when compared to the current 3D simulations and experimental observations.

G. Isotropy

Aiming to assess the isotropy properties of the flow at different length scales, we consider second-order velocity structure functions,

$$S^2_{i'}(T) = \langle |i'(x, y, z, t + T) - i'(x, y, z, t)|^2 \rangle_{y,t}, \qquad (7)$$

where $i = u, v, w$, T is the temporal increment, and $\langle \dots \rangle_{y,t}$ indicates averaging over the set of pointlike probes positioned at several locations along the centerline of the channel. Once again, the temporal increments have been converted to length increments by invoking Taylor's frozen hypothesis via the mean flow intensity, $X = TU$, where X is the increment in the streamwise direction. The results of our measurements showed that $S^2_{i'} \sim X^2$ (not shown here), meaning that the flow is smooth, which is consistent with spatial spectra being steeper than k^{-3}. To test the degree of isotropy of the flow and its scale dependence, we examine the ratio, $R = S^2_{u'}/S^2_{v'}$, for both 2D and 3D flows, reported in Fig. 13 as a function of the increment TU, and we extract data from several temporal probes and average as discussed above. Garg *et al.* [20] showed that in the limit of smooth flow at small increments ($TU \to 0$), the ratio R tends to 1/3 and 1/2, for 2D and 3D cases, respectively. While in the opposite, large-scale limit ($TU \to \infty$), the structure-function should reach a constant value. This can be attributed to a genuine decorrelation of velocity fluctuations beyond a given scale.

In the context of 2D simulations, our current results displayed in Fig. 13(a) indicate that isotropy is not restored at small scales. For all Wi values, the computed value of R significantly exceeds the expected theoretical value of 1/3 (depicted as the dashed black line). As anticipated, we detect anisotropic fluctuations at larger scales, as the data do not converge to the limit value of 1 [20]. Irrespective of Wi, the

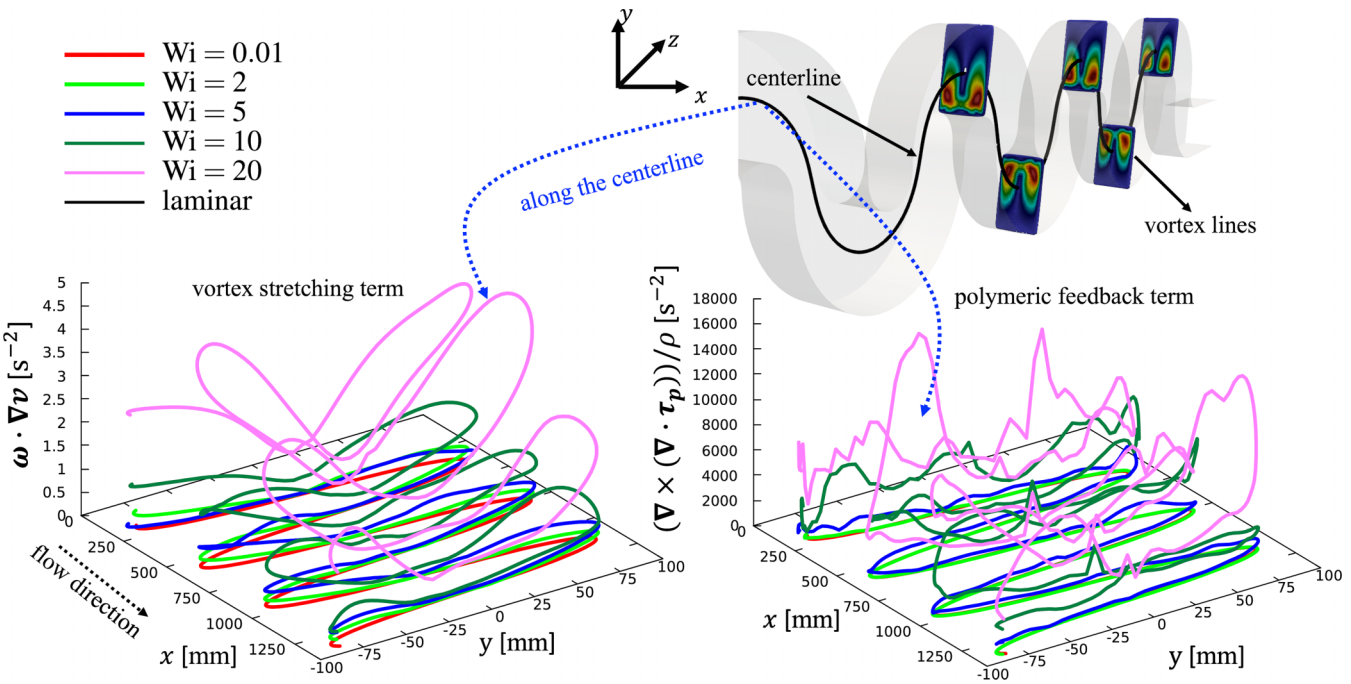

FIG. 9. Comparison of vortex stretching term, $\boldsymbol{\omega}\cdot\nabla\boldsymbol{v}$ and polymeric feedback term, $[\nabla\times(\nabla\cdot\boldsymbol{\tau_p})]/\rho$, as a function of Weissenberg number, Wi = 0.01–20, for 3D simulations. These results are extracted along the centerline of the channel (solid black line). Vortex lines are colored with vortex stretching magnitude.

isotropy ratio from our data converges to a limit of approximately $R \approx 0.65$. This limit is achieved for times exceeding the polymer relaxation time, λ, at which point velocity fluctuations become uncorrelated (correlations are not shown here). Qualitatively, our findings align with previous studies that have documented similar analyses [20]. However, when we examine the values of R in the 3D case [refer to Fig. 13(b)], a different narrative emerges. At small scales, there appears to be a decrease in the degree of anisotropy, while at larger scales, we still observe strong anisotropic fluctuations. Interestingly, the anisotropy in 2D seems to be more pronounced at small scales compared to 3D and the reason behind this is not trivial.

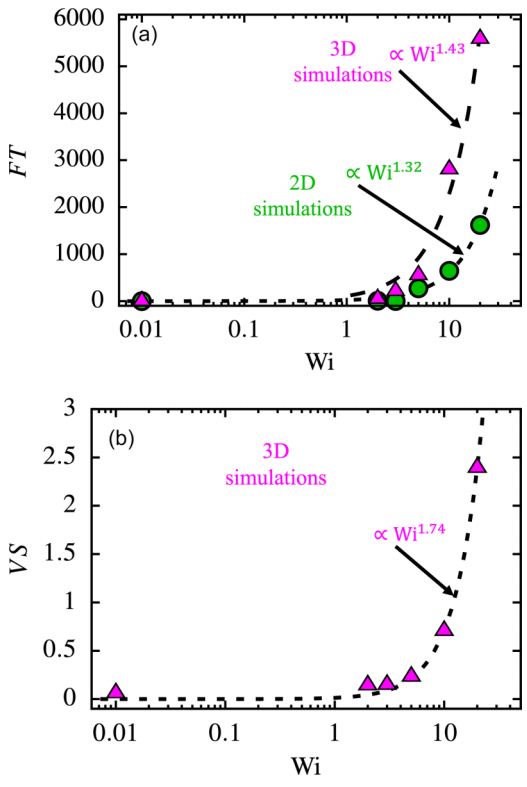

FIG. 10. Comparison of spatially averaged feedback term, FT [s^{-2}] and vortex stretching term, VS [s^{-2}] as a function of Wi number.

In contrast, in 3D, the fluid motion is not constrained to a single plane, and the vorticity of the flow can be more complex and isotropic due to lower degrees of in polymer alignment and stretching. To study this in more detail, we investigated the Lumley triangle [41], a graphical representation of the relationship between turbulent stresses, Reynolds stresses, and viscous stresses. The net anisotropy of the Reynolds stresses is commonly quantified using the second, II_b, and third, III_b, invariants of the normalized anisotropy tensor, b_{ij}, given by

$$b_{ij} = \frac{\langle\overline{u_i'u_j'}\rangle}{\langle\overline{u_k'u_k'}\rangle} - \frac{1}{3}\delta_{ij}. \tag{8}$$

The state of anisotropy can then be characterized with the two variables η and ξ defined as

$$\eta^2 = -\tfrac{1}{3}\mathrm{II}_b \tag{9}$$

and

$$\xi^3 = -\tfrac{1}{2}\mathrm{III}_b. \tag{10}$$

All realizable states of the Reynolds stress tensor are contained within a triangle in the (ξ,η) plane. All special turbulence cases can be characterized by the two invariants

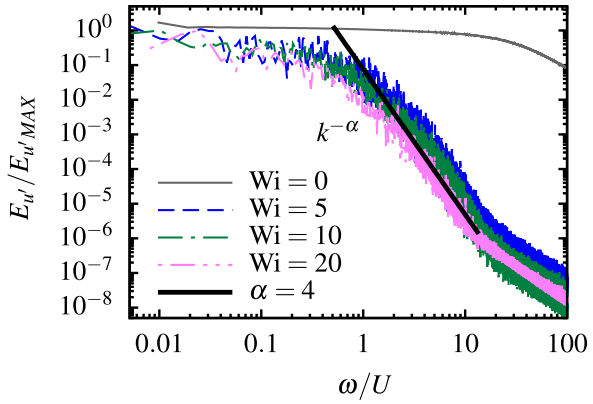

(a) $E_{u'}/E_{u'MAX}$ (2D simulations)

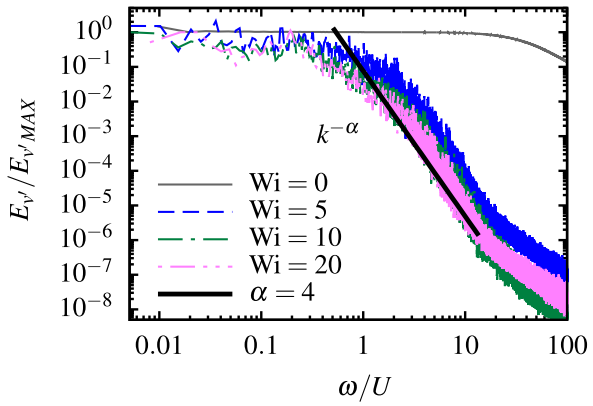

(b) $E_{v'}/E_{v'MAX}$ (2D simulations)

FIG. 11. Temporal spectra of velocity fluctuations [(a) and (b)] 2D simulations obtained from pointlike probes located at fifteen different positions in the channel for Wi = 5, 10, and 20. Here $\omega = 2\pi f$, f is the frequency, and U is the mean flow intensity. All spectra are normalized by their maximum values.

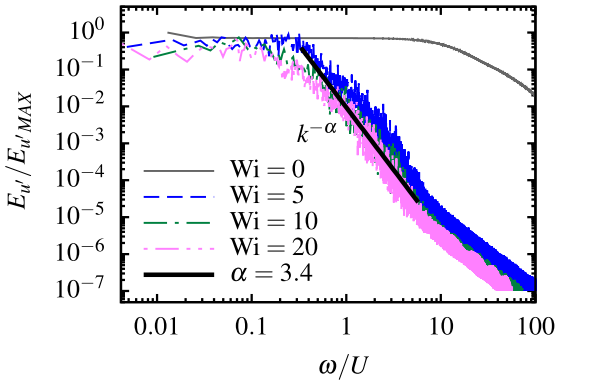

(a) $E_{u'}/E_{u'MAX}$ (3D simulations)

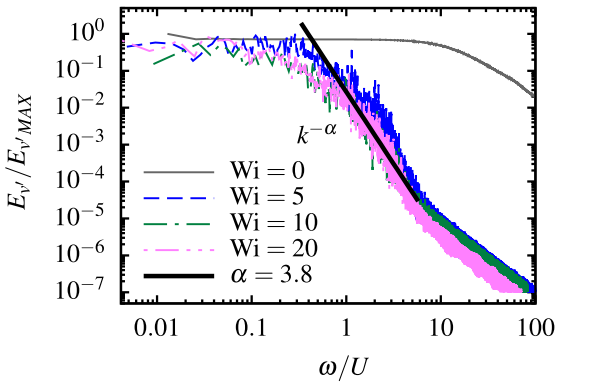

(b) $E_{v'}/E_{v'MAX}$ (3D simulations)

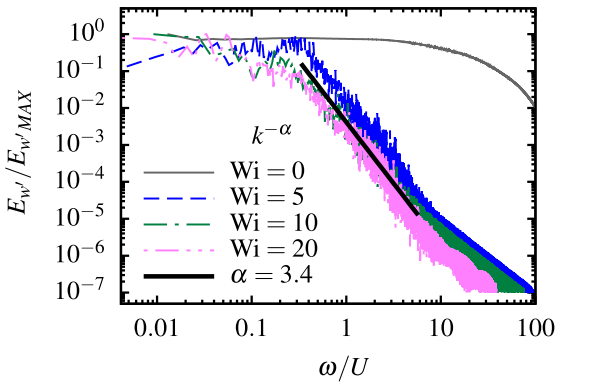

(c) $E_{w'}/E_{w'MAX}$ (3D simulations)

FIG. 12. Temporal spectra of velocity fluctuations [(a)–(c)] 3D simulations obtained form pointlike probes located at fifteen different positions in the channel for Wi = 5, 10, and 20. Here $\omega = 2\pi f$, f is the frequency, and U is the mean flow intensity. All spectra are normalized by their maximum values.

of b_{ij} at the theoretical limits of the Lumley triangle. Details on the different realizable states can be found in Garg *et al.* [42]. Lumley triangle plots for 3D viscoelastic flow in the micro serpentine channel are shown in Fig. 14 as a function of Wi number. All cell-centered values of ξ and η are postprocessed using PDF and represented with a colormap to match the trace of the polymer conformation tensor. In the limit of infinitely small Wi < $\mathrm{Wi_{crit}}$, we found that, in a laminar regime, the flow is close to a two-component state following the upper boundary of the Lumley triangle toward the one-component state denoted by the upper right corner. Interestingly, the curve never approaches the state of isotropy, which is at the bottom summit of the Lumley triangle. On the other hand, with the onset of elastic instabilities, these turbulent states are spread throughout the Lumley triangle with the exception of the plain strain condition indicated by the dashed line. More specifically, these turbulent states seem to form a spiral structure (also seen in experiments [9]), which starts from the two-component state, approaches towards the one-component state, and then keeps on oscillating between the oblate-axisymmetric and prolate-axisymmetric states before approaching the state of full isotropy. The prolate state corresponds to a flow with elongated structures aligned in the direction of the mean shear, while the oblate state corresponds to a flow with flattened turbulent structures aligned perpendicularly to the mean shear.

In our opinion, this behavior depends on the complex interplay of the serpentine channel geometry, flow conditions, and polymer relaxation time. However, here, we tried to interpret this in terms of polymer relaxation time. When the relaxation time of the polymer is small compared to the characteristic

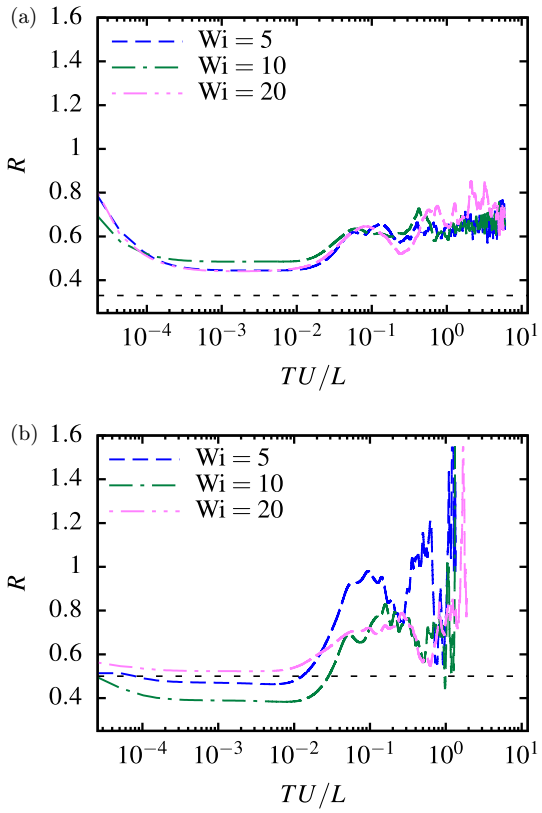

FIG. 13. Isotropy ratio, $R = S_u^2/S_{v'}^2$, versus the spatial increment obtained via the normalized mean flow intensity, TU/L, for (a) 2D and (b) 3D, for Wi = 5, 10, and 20. The horizontal dashed black line corresponds to the values of $R = 1/3$ and $R = 1/2$, representing isotropic conditions in 2D and 3D cases, respectively [20].

timescales of the flow, the polymer molecules relax quickly to their equilibrium configuration and damp out any fluctuation in the flow. Therefore, in this case, the flow behaves like a Newtonian fluid, and the Lumley triangle is in between the two- and one-component states. This is slightly different from plane channel flow, and the reason is the presence of strong curvature. However, when the relaxation time of the polymer is large compared to the characteristic timescales of the flow, i.e., $\mathrm{Wi} > \mathrm{Wi}_{\mathrm{crit}} \sim 2$, the polymers cannot relax fast enough to damp out fluctuations in the flow. This leads to a coupling between the fluid velocity and the polymer dynamics, which can result in highly complex and intermittent flow behavior. In summary, we could refer to it as a polymer memory effect, which refers to the ability of polymers to remember their previous deformations and to respond to subsequent deformations in a nonlinear way. This is one of the main reasons why our results show oscillation between axisymmetric prolate and axisymmetric oblate states on the Lumley triangle. The strength of the oscillation may become more pronounced as the polymer relaxation time increases, which means a stronger coupling between the fluid velocity and polymer dynamics.

It is important to note that the degree of anisotropy in both 2D and 3D also depends on a range of factors, including the specific flow geometry, flow conditions, etc. Therefore, more studies are required to verify our interpretation of turbulent states in elastic turbulent flows.

V. CONCLUSIONS

This study aims to provide a direct comparison between 2D and 3D simulations of elastic turbulence. It is the first to systematically investigate the statistical properties of a smooth random flow of a dilute polymer solution in 2D and 3D microserpentine channels, using numerical simulations at very low Reynolds (Re) and high Weissenberg (Wi) numbers, finding differences and similarities between the two for the first time. When looked on spatial flow statistics such as $\mathrm{tr}(\boldsymbol{\sigma})$, ω_z, and $\|\boldsymbol{D}\|$, only subtle differences between the 2D and 3D simulations are observed. Still, we do observe a difference in the critical Weissenberg number, with $\mathrm{Wi}_{\mathrm{crit}}^{\mathrm{3D}} < \mathrm{Wi}_{\mathrm{crit}}^{\mathrm{2D}}$. Below the onset of purely elastic instability, three distinguished regions of shear, extensional, and rotational behavior are visible, alternating orderly between successive half-bends. This suggests that polymers remain mainly in their coiled configuration, and thus, the flow is predominantly laminar. In the case of 3D simulations, these well-defined regions are no longer distinguishable for $\mathrm{Wi} > \mathrm{Wi}_{\mathrm{crit}}$, and the flow types are rather randomly distributed. This random distribution of flow types, combined with their impact on polymer behavior, results in spatial nonhomogeneity of the flow. However, this phenomenon is not observed for 2D.

For $\mathrm{Wi} > \mathrm{Wi}_{\mathrm{crit}}$, the onset of the time-dependent elastic instability leads to irregular flow patterns that result in the elastic turbulence regime. In this regime, the power spectra decay according to a power law, with the power law exponent α being 4 for 2D flows and 3.1–3.4 for 3D flows. We find that the results for 3D flows are closer to the experimental results than the results for 2D simulations. In addition, the geometry-induced mixed flow type and the strong rotation and weak extension of the flow in the turbulent state further reduce the extent of polymer stretching and, thus, reduce the range of excited scales in the turbulent flow.

Our results indicate that the 2D flow is highly anisotropic at all scales, while the 3D flow tends to approach an isotropic state at small scales but remains highly anisotropic at large scales. Interestingly, we use the Lumley triangle to explore the possibility of different elastic turbulence states in 3D serpentine channels, even in the presence of weaker elastic instabilities. We find that a coexistence of axisymmetric-prolate and -oblate states occurs due to the polymer memory effect for $\mathrm{Wi} \geqslant \mathrm{Wi}_{\mathrm{crit}}^{\mathrm{3D}}$.The emergence of a spiral vortical pattern becomes readily apparent once elastic instabilities begin to manifest, in alignment with the findings observed in the experimental study conducted by Soulies *et al.* [9].

When examining the vorticity transport equation, a direct comparison between vortex stretching and the polymeric feedback term reveals intriguing findings, notably highlighting the predominance of the polymeric feedback term over vortex stretching. Through data fitting, we discovered that the feedback term scales with Wi^b in both 2D and 3D cases, albeit with different scaling exponent, i.e., $b = 1.32$ for 2D and $b = 1.43$ for 3D, respectively. This comparison emphasizes that the primary driver of elastic instability is the curvature of streamlines induced by the flow geometry, rather than the relatively weaker secondary flow in the azimuthal direction.

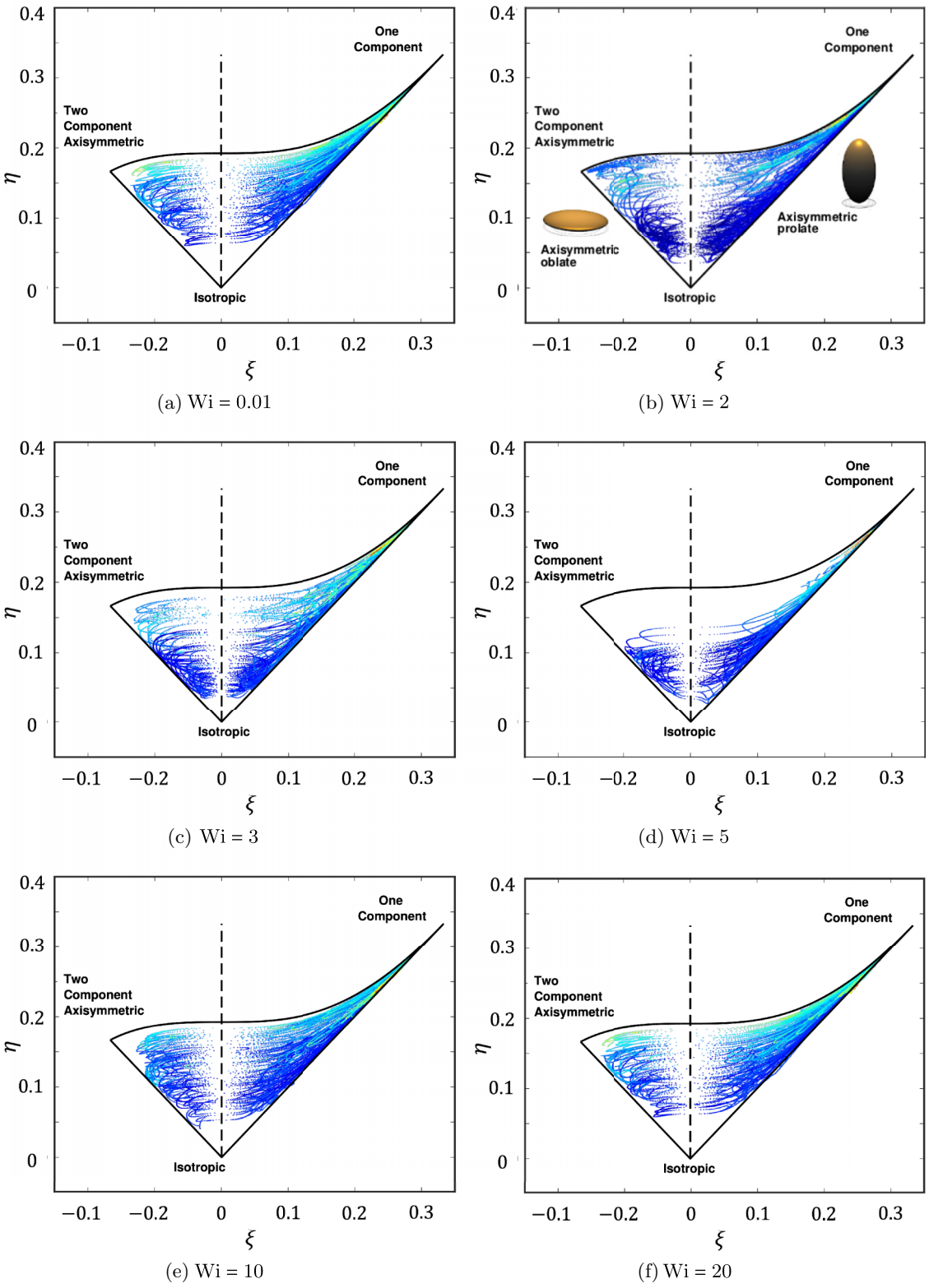

(a) Wi = 0.01 (b) Wi = 2

(c) Wi = 3 (d) Wi = 5

(e) Wi = 10 (f) Wi = 20

FIG. 14. Anisotropy-invariant mapping of 3D turbulence in microserpentine channel viscoelastic flow compiled from the present DNS data at different Wi numbers. The data points for each case are based on all cells in the domain and colored with tr($\boldsymbol{\sigma}$) values. Color map varies from blue (minimum) to red (maximum).

In conclusion, as shown by the results, while 2D simulations can qualitatively replicate certain aspects observed in 3D simulations, there are notable quantitative disparities. The absence of vortex stretching in 2D simulations leads to an underestimation of various flow parameters such as the topology factor, velocity fluctuation magnitude, polymeric energy, and polymeric feedback magnitude. These parameters are crucial for optimizing heat exchanger

designs, industrial mixing processes, thermal management systems, and processes involving heat transfer in viscoelastic fluids. Therefore, despite their extensive use in studying elastic turbulence, 2D simulations should be approached with caution.

The data that support the findings of this study are available from the corresponding author on reasonable request.

ACKNOWLEDGMENTS

The authors greatly appreciate the Swedish National Infrastructure for Computing (SNIC) for providing the Computer time, partially funded by the Swedish Research Council through Grant No. 2018-05973.

The authors have no conflicts of interest to disclose.

[1] R. Benzi and E. S. Ching, Annu. Rev. Condens. Matter Phys. **9**, 163 (2018).
[2] F. Del Giudice, G. D'Avino, F. Greco, I. De Santo, P. A. Netti, and P. L. Maffettone, Lab Chip **15**, 783 (2015).
[3] Z. Zhang, X. Wang, and Y. Yan, e-Prime. Adv. Electr. Eng. Electr. Energy **1**, 100009 (2021).
[4] A. Groisman and V. Steinberg, Nature (London) **405**, 53 (2000).
[5] A. Groisman and V. Steinberg, Nature (London) **410**, 905 (2001).
[6] A. Groisman and V. Steinberg, New J. Phys. **6**, 29 (2004).
[7] T. Burghelea, E. Segre, I. Bar-Joseph, A. Groisman, and V. Steinberg, Phys. Rev. E **69**, 066305 (2004).
[8] T. Burghelea, E. Segre, and V. Steinberg, Phys. Fluids **19**, 053104 (2007).
[9] A. Soulies, J. Aubril, C. Castelain, and T. Burghelea, Phys. Fluids **29**, 083102 (2017).
[10] P. C. Sousa, F. T. Pinho, and M. A. Alves, Soft Matter **14**, 1344 (2018).
[11] S. Berti, A. Bistagnino, G. Boffetta, A. Celani, and S. Musacchio, Phys. Rev. E **77**, 055306(R) (2008).
[12] H. Garg, Ph.D. thesis, 2019, http://www.theses.fr/2019LILUI003.
[13] V. Steinberg, Annu. Rev. Fluid Mech. **53**, 27 (2021).
[14] B. Traore, C. Castelain, and T. Burghelea, J. Non-Newtonian Fluid Mech. **223**, 62 (2015).
[15] W. Abed, R. Whalley, D. Dennis, and R. Poole, J. Non-Newtonian Fluid Mech. **231**, 68 (2016).
[16] J. Mitchell, K. Lyons, A. M. Howe, and A. Clarke, Soft Matter **12**, 460 (2016).
[17] A. Fouxon and V. Lebedev, Phys. Fluids **15**, 2060 (2003).
[18] S. Berti and G. Boffetta, Phys. Rev. E **82**, 036314 (2010).
[19] H. Garg, E. Calzavarini, G. Mompean, and S. Berti, Eur. Phys. J. E **41**, 115 (2018).
[20] H. Garg, E. Calzavarini, and S. Berti, Phys. Rev. E **104**, 035103 (2021).
[21] R. van Buel, C. Schaaf, and H. Stark, Europhys. Lett. **124**, 14001 (2018).
[22] R. Van Buel and H. Stark, Phys. Fluids **34**, 043112 (2022).
[23] J. Zilz, R. J. Poole, M. A. Alves, D. Bartolo, B. Levaché, and A. Lindner, J. Fluid Mech. **712**, 203 (2012).
[24] R. Bird, C. Curtiss, R. Armstrong, and O. Hassager, *Dynamics of Polymeric Liquids, Volume 2: Kinetic Theory* (Wiley, New York, 1987).
[25] J. Oldroyd, Proc. R. Soc. Lond. A **200**, 523 (1950).
[26] R. J. Poole, M. A. Alves, and P. J. Oliveira, Phys. Rev. Lett. **99**, 164503 (2007).
[27] F. Pimenta and M. Alves, RheoTool (2016), https://github.com/fppimenta/rheoTool.
[28] H. G. Weller, G. Tabor, H. Jasak, and C. Fureby, Comput. Phys. **12**, 620 (1998).
[29] R. Fattal and R. Kupferman, J. Non-Newton. Fluid Mech. **123**, 281 (2004).
[30] M. Alves, P. Oliveira, and F. Pinho, Int. J. Numer. Methods Fluids **41**, 47 (2003).
[31] L. Ducloué, L. Casanellas, S. J. Haward, R. J. Poole, M. A. Alves, S. Lerouge, A. Q. Shen, and A. Lindner, Microfluid. Nanofluid. **23**, 33 (2019).
[32] H. Garg and L. Wang, arxiv:2304.04025.
[33] F. P. Incropera, D. P. DeWitt, T. L. Bergman, and A. S. Lavine, *Fundamentals of Heat and Mass Transfer* (Wiley, New York, 1996), Vol. 6.
[34] Y. Jun and V. Steinberg, Phys. Rev. E **84**, 056325 (2011).
[35] E. Balkovsky, A. Fouxon, and V. Lebedev, Phys. Rev. E **64**, 056301 (2001).
[36] V. Steinberg, Phys. Rev. Lett. **123**, 234501 (2019).
[37] E. S. G. Shaqfeh, J. Non-Newton. Fluid Mech. **130**, 1 (2005).
[38] J. S. Lee, R. Dylla-Spears, N. P. Teclemariam, and S. J. Muller, Appl. Phys. Lett. **90**, 074103 (2007).
[39] P. Shakeri, M. Jung, and R. Seemann, Phys. Fluids **34**, 073112 (2022).
[40] D. Y. Li, H. Zhang, J. P. Cheng, X. B. Li, F. C. Li, S. Qian, and S. W. Joo, Microfluid. Nanofluid. **21**, 1 (2017).
[41] S. B. Pope, *Turbulent Flows* (Cambridge University Press, Cambridge, 2000).
[42] H. Garg, L. Wang, M. Andersson, and C. Fureby, Physics of Fluids **36**, 045138 (2024).